Test Summary of the NASA Semi-Span High-Lift Common Research Model at the QinetiQ 5-Metre Low-Speed Wind Tunnel

Ashley Evans[1]
Boeing Defence UK, Ltd., Salisbury, Wiltshire, SP4 0JF, United Kingdom

Doug Lacy[2]
The Boeing Company, Seattle, WA 98124

Ian Smith[3]
QinetiQ Ltd, Farnborough, Hampshire, GU14 0LX, United Kingdom

Melissa Rivers[4]
NASA Langley Research Center, Hampton, VA 23681

A summary and selected results from experimental testing of the NASA 10% scale semi-span High-Lift Common Research Model (CRM-HL) at the QinetiQ 5m pressurized low-speed wind tunnel (5mWT) are presented. There were many objectives of this test, the primary being to collect data to define a set of reference landing and takeoff configurations for dissemination and use within the CRM-HL ecosystem. A database of force, moment, pressure and surface flow visualization data were collected to support several objectives: aerodynamic sensitivity to high-lift device positioning, Reynolds number effects on configuration selection, isolation of the effects of various components of the reference configuration (e.g. landing gear, nacelle, horizontal tail, etc.), and limited repeatability data for uncertainty quantification assessment. Some results were compared to data collected at the NASA Langley Research Center 14x22 Foot wind tunnel to assess half-model effects and facility differences. Half-model effects were further studied with the use of wind tunnel floor blowing to change the boundary layer profile and assess the effects on model aerodynamics. Flow visualization data were gathered with fluorescent mini-tufts and UV oil. Finally, initial demonstration and development of new Particle Image Velocimetry (PIV) and Model Deformation Measurement (MDM) capabilities at the 5mWT facility were performed.

---

[1] Aero Test Engineer, Boeing Test and Evaluation, AIAA Member
[2] Boeing Associate Technical Fellow, Flight Sciences, AIAA Associate Fellow
[3] Head of 5m Testing, QinetiQ Ltd, AIAA Member
[4] Subproject Manager, TTT Project, AIAA Associate Fellow

I. Nomenclature

$C_{L,max}$ = maximum lift coefficient
C_M = pitching moment coefficient
VG = vortex generator
c = local wing chord
g = gap, leading edge slat and trailing edge flap
h = height, leading edge slat
o = overlap, trailing edge flap
α_U = uncorrected angle of attack
η = fraction of wing semi-span

II. Introduction

While Computational Fluid Dynamics (CFD) has penetrated nearly every aspect of aerospace design and analysis, the extent to which it can be used to predict high-lift aerodynamic characteristics and therefore performance of a high-lift transport aircraft remains limited [1]. Validation exercises in the third High Lift Prediction Workshop (HLPW-3) show disagreement in lift, pitching moment and drag, with the widest spread of results at $C_{L,max}$ [2]. The flow characteristics that dominate high-lift performance, such as boundary layer transition, turbulence, separation, viscous wake interactions, and confluent flows are weaknesses of CFD modeling that require further development [3].

Given the inability to predict high-lift performance, industrial design is still largely dependent on wind tunnel testing. However, wind tunnel results are not without their own uncertainty, owing to wall effects [4], installation effects [5], Reynolds number scaling [6] and geometric modeling compromises. The aircraft designer must consider all of these when using wind tunnel data to predict full-scale flight characteristics.

To address these shortcomings and advance CFD capability along with wind tunnel accuracy, the purpose of the High-Lift Common Research Model (CRM-HL) ecosystem is to establish dialogue between computational and experimental researchers and practitioners [7]. By creating a common, systematic approach to the unique challenges of high-lift aerodynamics, both disciplines can improve the accuracy and collective precision of their predictions. For example, CFD can be improved through focused and intentional validation experiments, and wind tunnel methods can improve upon uncertainty quantification and data corrections with the help of CFD.

At the heart of the ecosystem is a common geometry that is publicly available for both computational and experimental users. Based on the high-speed CRM model [8], the first low-speed configuration was defined by Lacy and Sclafani [9]. Since then, NASA has built a 10% scale semi-span model for testing at the NASA Langley Research Center 14-by-22 foot atmospheric wind tunnel (14x22) [10, 11]. Though the focus of that test was to demonstrate active flow control, limited data were collected for the conventional high-lift configuration as well.

The subject of this paper is a test of the same physical model in the QinetiQ 5-metre wind tunnel (5mWT) located in Farnborough, UK. This test focused primarily on developing the reference configurations that will be used for all future CRM-HL work [12], and collecting data to support the ecosystem in the context of CFD validation and identifying wind tunnel areas of emphasis. The test was a joint project between NASA, Boeing, and QinetiQ and took place October 14th – November 15th 2019.

III. CRM-HL Test Campaign Overview and Objectives

The primary objective of the test was to develop a reference configuration for a nominal landing and a nominal takeoff configuration [12]. This was done by collecting position sensitivity data for the leading and trailing edge devices. Real-time force, moment, and surface pressure data coupled with real-time surface flow visualization in the form of fluorescent mini-tufts allowed for the test plan to be adapted as data were collected. Concurrently, data were collected to capture the aerodynamic sensitivity to high-lift device positioning about the configuration as it developed.

The following is a general sequence of test blocks and objectives fulfilled in each:

- Takeoff configuration check
  - First experimental verification of takeoff device positioning
  - Explore nacelle chine placement for takeoff performance
- Comparison with 14x22
  - Compare identical landing configuration for tie-in and assessment of facility differences

- o   Investigate half-model effects with floor blowing and floor VGs
- Landing configuration – trailing edge testing
  - o   Gather positioning sensitivities and refine pre-test configuration
- Landing configuration – leading edge testing
  - o   Gather positioning sensitivities and refine pre-test configuration
  - o   Establish common chine position for takeoff and landing
  - o   Assess effect of horizontal tail
  - o   Assess effect of main landing gear
- Landing configuration – Reynolds number and Mach variations
  - o   Assess the impact of Reynolds number and Mach number on new reference configuration
- PIV system development
  - o   Assess placement of laser and cameras for half-model
  - o   Assess seeding requirements for full circuit at 1-3 atmospheres
- MDM system development
  - o   Assess placement of infra-red cameras for half-model
  - o   Assess target placement and data reduction
- Takeoff configuration – leading edge testing
  - o   Gather positioning sensitivities and refine pre-test configuration
- Takeoff configuration – trailing edge testing
  - o   Gather positioning sensitivities and refine pre-test configuration
- Landing configuration – Reynolds number and flap deflection
  - o   Assess the impact of Reynolds number on optimum flap deflection
  - o   Assess in-test data repeatability
- UV oil studies
  - o   Gather data for landing configuration with varying Reynolds number
  - o   Gather data for nacelle and pylon removed
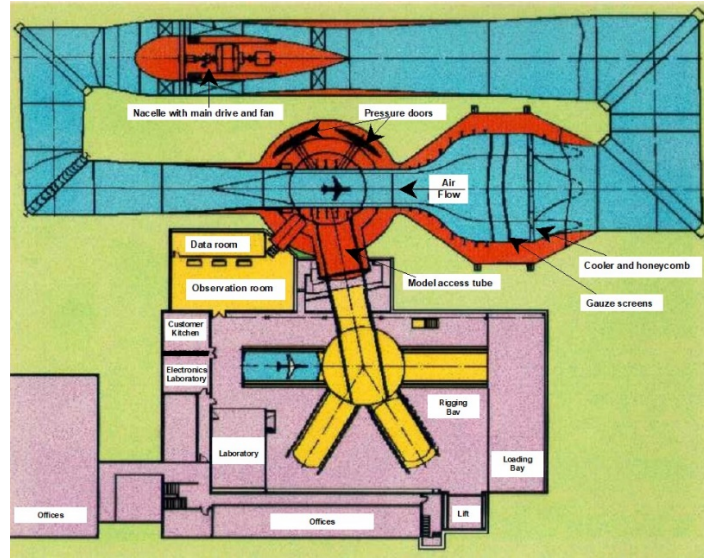
IV.   Facility Overview

The QinetiQ 5mWT is a closed-circuit return facility which can be pressurized to 3 atmospheres and achieve Mach numbers up to 0.3 with a model installed. It is powered by an AC and a DC electric motor which drive the single-stage fan. The motors are housed inside a nacelle located within the tunnel circuit. An adjacent compressor plant provides pressurization and maintains pressure during wind-on. The tunnel control system provides three modes of operation, controlling for either constant Mach number, constant dynamic pressure or constant Reynolds number. A water cooling system maintains temperature within the circuit, usually around 70-75° F. The facility is constructed so that access to the test section is available while the rest of the circuit remains pressurized. The tunnel test section is enclosed within the inner of two concentric spheres, with the outer sphere permanently connected to the tunnel circuit, and remaining at the tunnel operating pressure. Test section access is achieved by pneumatically isolating the inner sphere using pressure doors at each end of the test section, allowing depressurization of the test section only while pressure is held in the rest of the circuit. A general layout of the facility is presented in Figure 1.

The octagonal test section is 4.2m tall by 5m wide by 12m long. It has straight, solid walls, with corner fillets that are tapered, growing smaller towards the downstream end to ensure negligible static pressure gradient. Mean longitudinal turbulence intensity is 0.08% and flow uniformity is good, there being only a few regions near the walls where the dynamic pressure is greater than ±0.1% of the centerline value. Upstream of the test section is a rapid diffuser, followed by a settling chamber with the cooler, a honeycomb section and two gauze screens, and finally a contraction with ratio 7.64 [13]. A floor-blowing system for boundary layer control is located forward of the test section, and mass flow through the slot is modulated by input and bypass valves. At one time the blowing system had an associated mass-flow measurement setup, but as the system had not been used for many years, it was not available for this test. Therefore, a removable boundary layer rake was located forward and starboard of the model so that blowing-on conditions could be roughly repeated by monitoring velocity profiles from the rake.

Tunnel blockage and induced upwash corrections are calculated using a suite of pressure taps that are located on the tunnel walls, shown in Figure 2. Angle-of-attack is corrected with a mean upwash calculation across the span of the wing, and force and moment coefficients are calculated by resolving the measured balance loads into the corrected

axis system and applying corrected dynamic pressure. Corrected data from the balance and pressure data from the model are available for real-time plotting. Once the raw data are gathered, the online data processing software applies the corrections and the processed data are available to view after each point.

A detailed survey of the test section onset flow is to be completed in 2021. The data will be provided to the CFD community, along with the tunnel and model geometries, to allow theoretical calculations to be compared to the experimental data from this test.

Figure 1: General layout of QinetiQ 5mWT facility
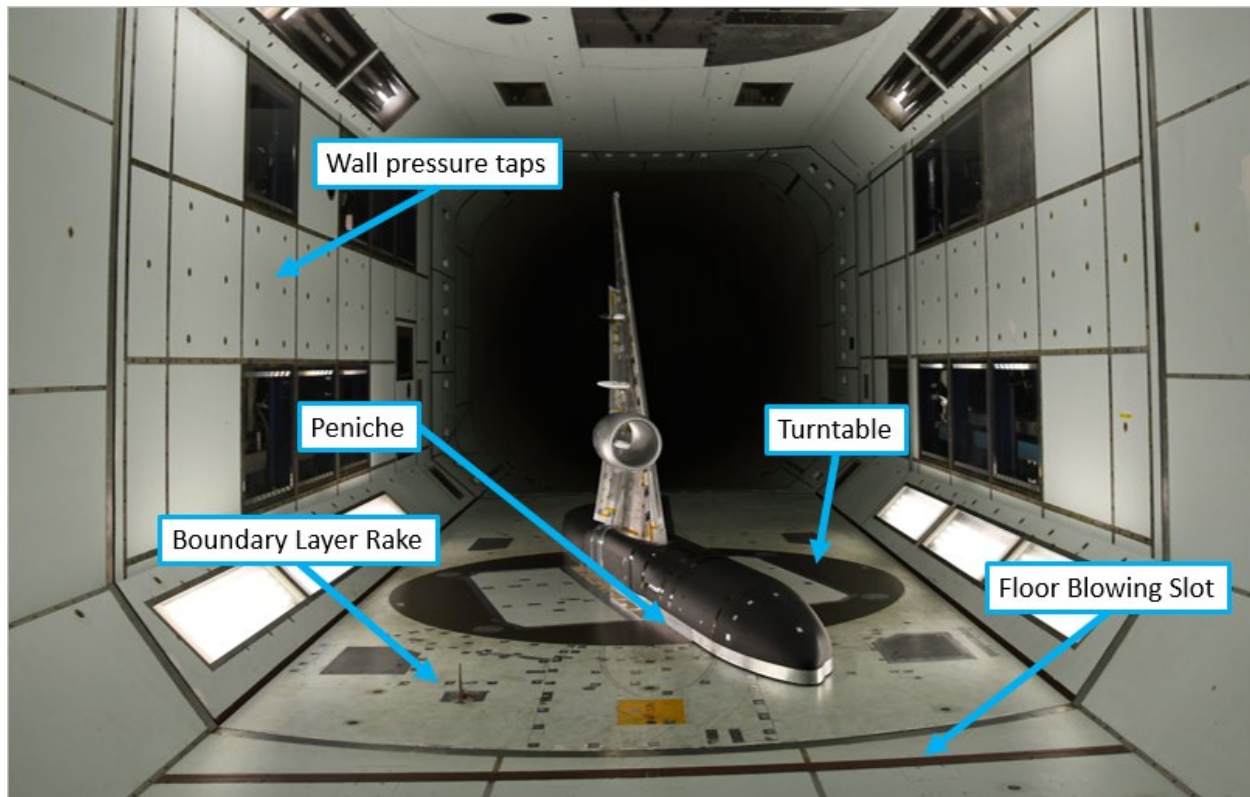
Figure 2: 10% CRM-HL installed in the QinetiQ 5mWT

V. Model Overview

A. Configuration

The model is a right-hand side semi-span model with a half-fuselage, a wing spar, leading edge slats, a wing under-slat surface (WUSS), a flow-through nacelle, nacelle pylon, trailing-edge flaps, flap track fairings, removable main landing gear, and a removable horizontal tail. In general, all parts were designed to strike a balance between modeling a real-world modern transport aircraft and a geometry that is simplified for CFD and manufacturing purposes. Figure 3 gives an overview of the model layout.

The outboard slat is a single piece, with brackets laid out to simulate six individual slats with two brackets each. The inboard slat is also a single piece with three brackets. Brackets are similar in number, location and width to modern airliners. However, dissimilar from an airliner, the brackets attach to the lower surface of the wing aft of the major curvature area of the WUSS as opposed to extending through the area of high curvature. This was done to provide a configuration more easily replicated on future wind tunnel models and in CFD. The brackets attach to the wing inside of inset pockets, which are covered with a plastic cover to preserve the lower surface shape.

Slat placement is defined in terms of height, gap and deflection, as defined in Figure 4. The height is adjusted with shims placed under the wing-side foot of the bracket, and is measured from the wing reference plane to the upper surface trailing edge of the slat, normal to the wing reference plane. The gap is infinitely adjustable with slotted fastener holes on the wing-side foot of the bracket, and is defined as the shortest distance between the WUSS and the slat. The deflection is built into the bracket itself, and so multiple brackets with different deflections were used. Details of the outboard leading edge are presented in Figure 5. For this preliminary geometry, leading edge slat deflection is measured around a rotation axis for each slat for the initial nominal takeoff and landing positions of 22 and 30 degrees, respectively. Additional positions were defined by rotating the slats plus and minus three degrees around a straight line representation of the respective slat trailing edges. In doing so, the height and gap distributions were essentially unchanged as the angle was varied.

The single-slotted fowler flaps are attached to the wing with two brackets each, positioned span-wise to mimic the flap support locations of many modern commercial transport aircraft. The inboard bracket of the inboard flap is mounted inside the fuselage. The remaining brackets are wing-mounted and are covered by hollow flap track fairings. These fairings have not been designed for high speed performance, but rather only to represent the approximate size and produce the low speed aerodynamic impact of typical flap support fairings. These fairings are split into forward and aft elements at approximately the local stowed flap leading edge. The forward end is attached to the wing main element, while the aft portion is deflected downward about a hinge line near the bottom of the fairing near where it is split. The amount of aft fairing rotation is dependent on flap angle and is selected to provide for some flap gap and overlap adjustment. Details of the inboard trailing edge are presented in Figure 6.

Flap placement is defined by gap, overlap, and deflection, as shown in Figure 4. Gap is set using shims under the wing-side foot of the bracket and is defined as the shortest 3-dimensional distance between the lower surface trailing edge of the spoilers and the flap. Overlap is adjustable with slotted fastener holes at the wing-side foot of the bracket and is defined as the longitudinal (x-direction) distance between the flap leading edge and the spoiler trailing edge. Deflection is built into the bracket itself, and so multiple brackets with different deflections were used. Deflection is stream wise and defined in the wing coordinate system.

The quantities gap, overlap, and height are non-dimensionalized to g/c, o/c and h/c using a reference chord. For the slats and outboard trailing edge, this is the local chord of the trapezoidal wing (which excludes the contribution of the inboard wing trailing edge extension). For the inboard trailing edge, reference chord is a constant defined as the wing chord at the wing trailing edge break.

In the design and fabrication of the wind tunnel model, an error was made that led to the spoiler trailing edges being misaligned at their junction on the order of ~0.1" model scale (Figure 7). Essentially, the outboard spoiler had been trimmed too far forward. However, in the NASA test, the flap was positioned as if the spoiler had been correctly trimmed, with the result being a smaller than intended overlap and larger than intended gap for the flap. This scenario was replicated at QinetiQ for runs intended for tunnel to tunnel comparisons. For all other testing, the outboard flap was set to intended gaps and overlaps behind the incorrectly trimmed spoiler which resulted in a small mismatch with the inboard flap at their junction. As aircraft flaps typically have some degree of sealing at their flap-to-flap interfaces, similar sealing was represented on the model using a moldable filler and reinforced with tape on the lower surface. The amount of chord-wise sealing was decreased with increasing flap deflection as is typical with flaps of differing sweep angles.

All suction surfaces, namely the upper surface of the wing, slats, and flaps, were designed to be as smooth as possible, minimizing fastener holes and other discontinuities. On the lower surface, these holes were covered with

tape. Where they appear on the upper surface, these holes were smoothly filled. The slots in the slat bracket covers that enabled gap adjustability were covered with tape. Similarly, fastener holes on the fuselage were covered.

The forward portion of the flap penetrates the fuselage, and inside is held with a bracket similar to the on-wing brackets. An oversized cutout in the fuselage is required at this penetration in order to permit flap adjustability. However, the resulting gap around the flap was sealed with filler and tape to prevent leakage paths. Additionally, a small amount of filler was placed all around the wing root to maintain sealing.

The nacelle is a single-element flow-through nacelle mounted on a simplified pylon. The leading edge of the nacelle is identical to the high-speed version of the CRM, which will be relevant to results discussed later. A chine was mounted to the inboard side of the crown of the nacelle. This is a plastic piece that is 3D printed with feet that are taped to the nacelle. Multiple sizes and positions were tested. The placement of the nacelle chine is defined with respect to a reference point (the corner of the side panel) in inches along the radial and longitudinal directions (Figure 8). All chine installations included a nose-down angle to approximate a typical airplane orientation.

Pressure tap routing into the leading and trailing edge devices was accomplished in a non-intrusive fashion. Leading edge tubing was routed through channels in the underside of the brackets. Tubing for the outboard flap was routed within the fairings that covered the flap brackets. Tubing for the inboard flap was routed directly into the body through the portion of flap that penetrated the body to reach the internal inboard flap bracket.
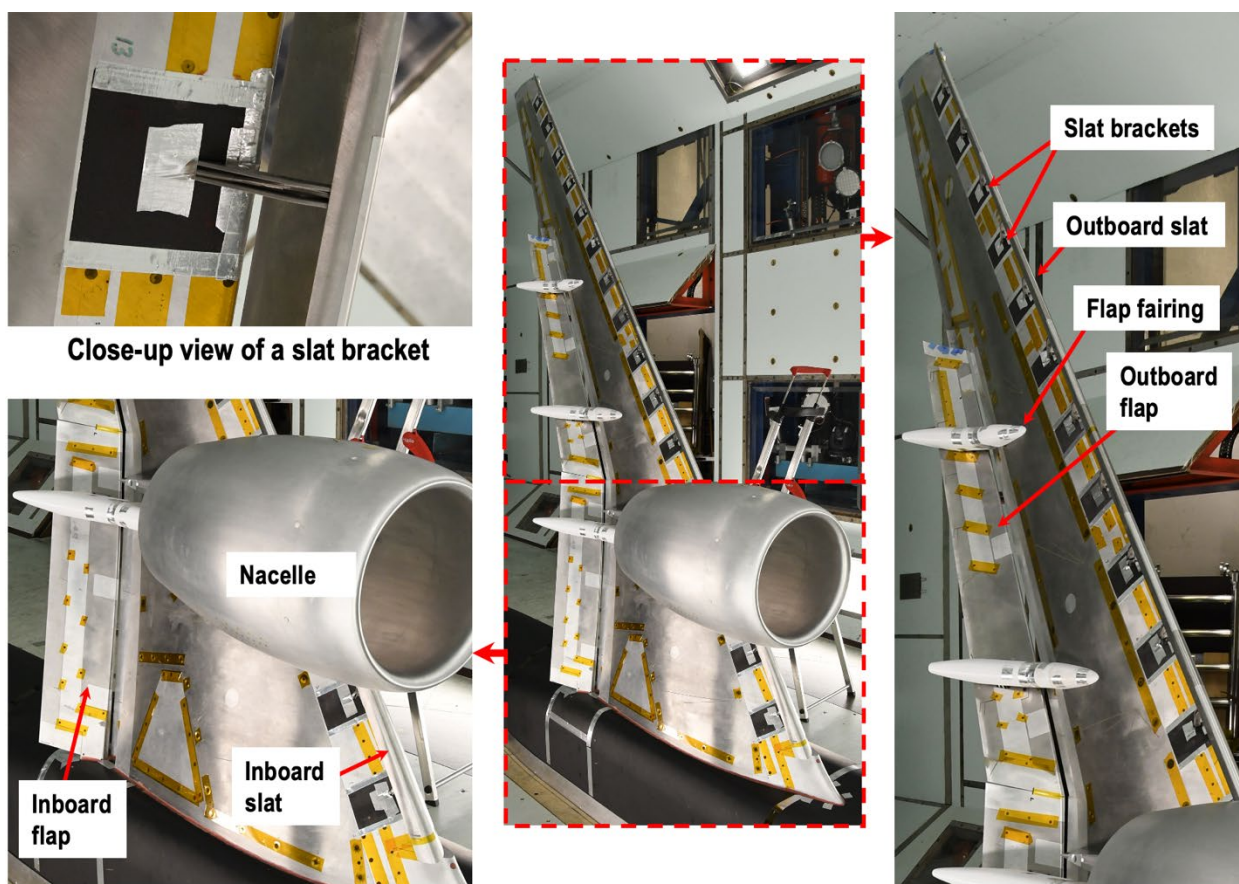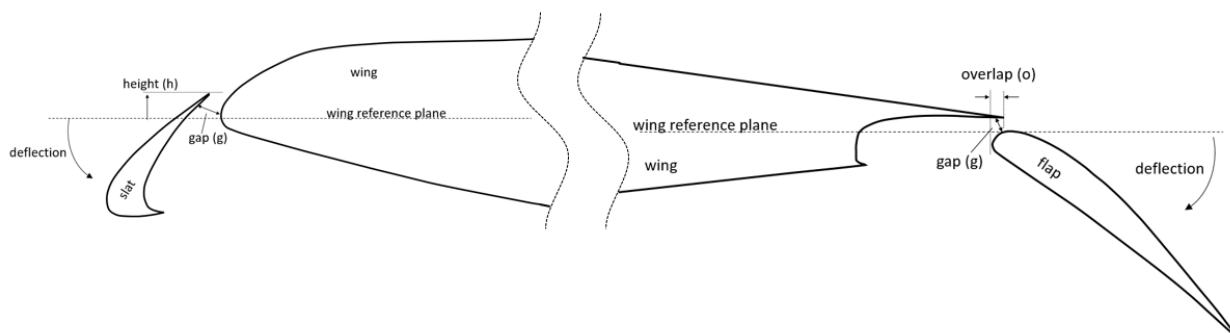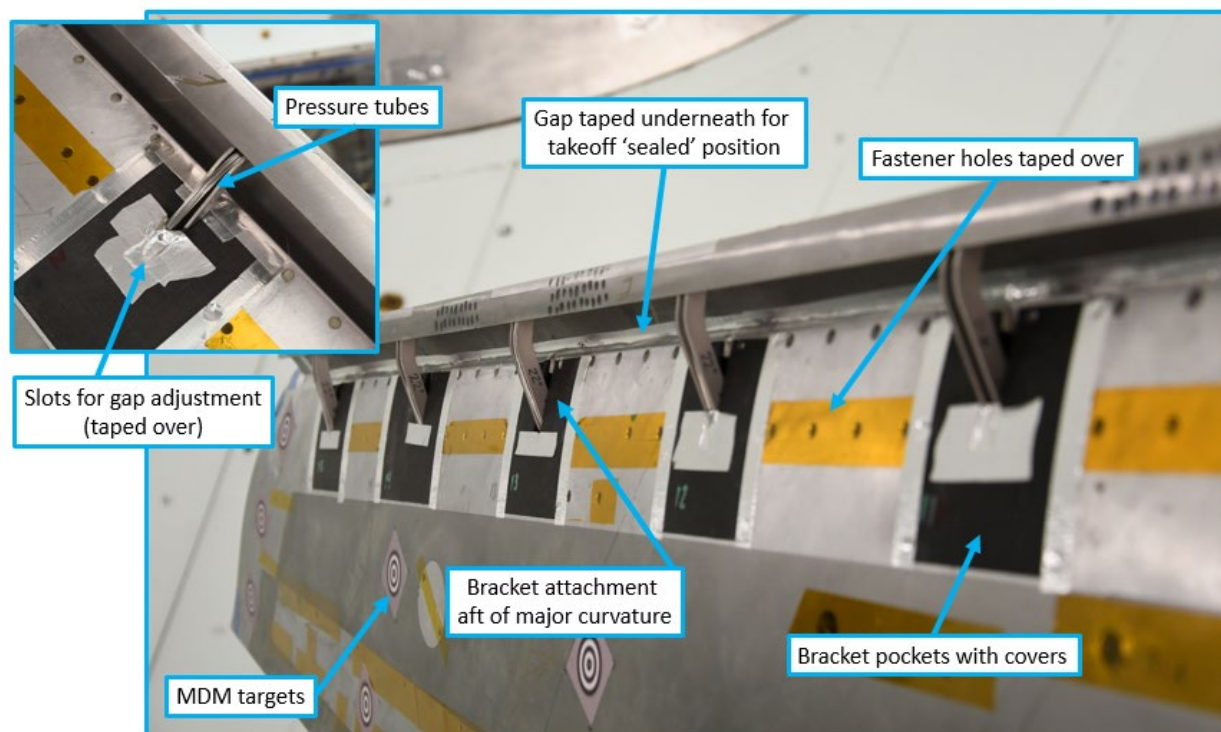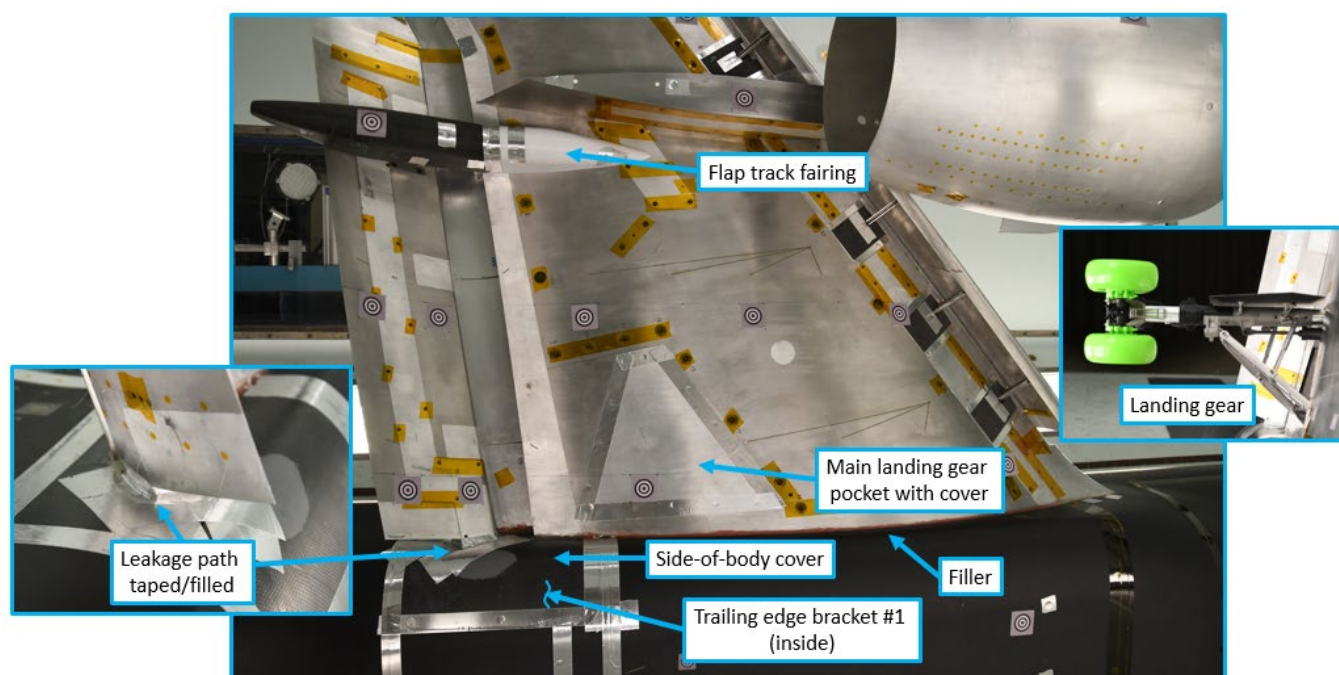
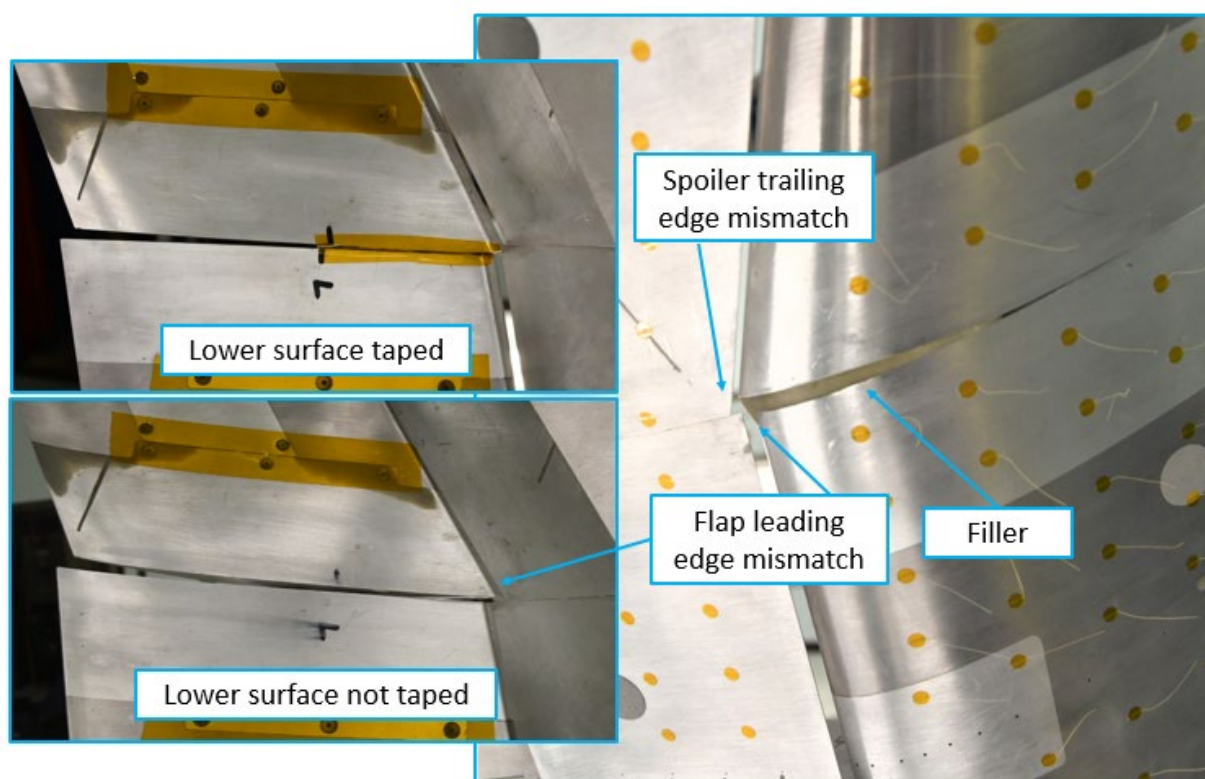

Figure 3: General model layout

6

Figure 4: High-lift system position definitions
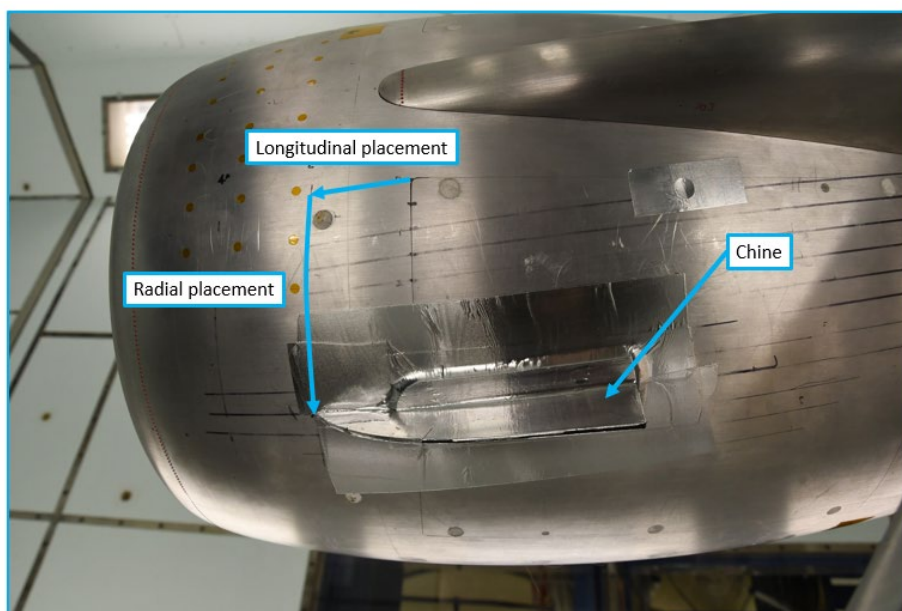

Figure 5: Outboard leading edge detail

Figure 6: Inboard trailing edge and side of body


Figure 7: Flap juncture

Figure 8: Nacelle chine placement

B. Installation

The CRM-HL model was mounted on QinetiQ's underfloor six-component weigh beam balance. The balance integrates with the non-metric turntable, which is usually configured to provide a rotation of ±30°, though for this test only angles of attack from zero to 28° were used. Data are collected using a pitch-pause method, where time is allowed between each data point for the balance to stabilize.

The model was installed in the tunnel using an adapter block to mount the model to the balance. The adapter block was designed to position the model ~3.3 inches above the tunnel floor to accommodate the peniche. The peniche, shown in Figure 9, serves as a standoff between the model and the tunnel floor, and forms the lower half of a labyrinth seal within the model. Available data indicated that the expected floor boundary layer thickness would be similar between the two facilities, so the same peniche height was utilized for both tunnels. Where the model overhangs the turntable, a brush seal was used to minimize airflow underneath the fuselage while at the same time preventing interference between the stationary floor and the model. The peniche was custom built for the 5mWT test as the turntable is smaller than that used during the 14x22 test.
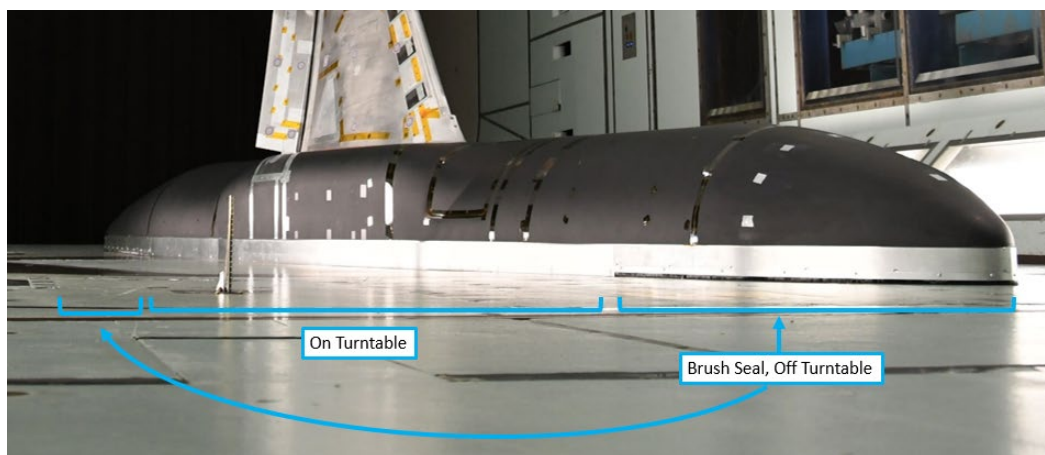
Figure 9: Peniche installation

C. Instrumentation and Flow Visualization

The model was fitted with 730 static pressure ports across the wing and body and 20 on the tail. The ports are located in stream-wise and span-wise rows spread across the wing, in circumferential rows along the fuselage, and in stream-wise and circumferential rows on the nacelle, as shown in Figure 10. With every pitch-pause data point, all pressure ports were digitally scanned by the 5mWT's TE Connectivity Optimus pressure measurement system, which has data rates up to 2kHz, and time-averaged over 8 seconds to generate a single value for each port. The reliability of the pressure port data was an issue throughout the test due to electronic pressure scanner issues as well as occasional plugged ports and damaged tubes. All issues with pressure port data were monitored and maintained throughout the test, but some invalid points in the dataset were unavoidable.

Surface flow visualization data were gathered using fluorescent mini tufts, illuminated by high-energy lights and captured by high-definition cameras at every point in the pitch sweep. Still photos and video of flow visualization data were available for real-time assessments of the flow characteristics. Images of UV oil patterns were captured for dedicated UV oil runs.

The model is equipped with dynamic pressure sensors (kulites) for unrelated testing; these were not utilized for this test and were covered with tape for the duration of the test.
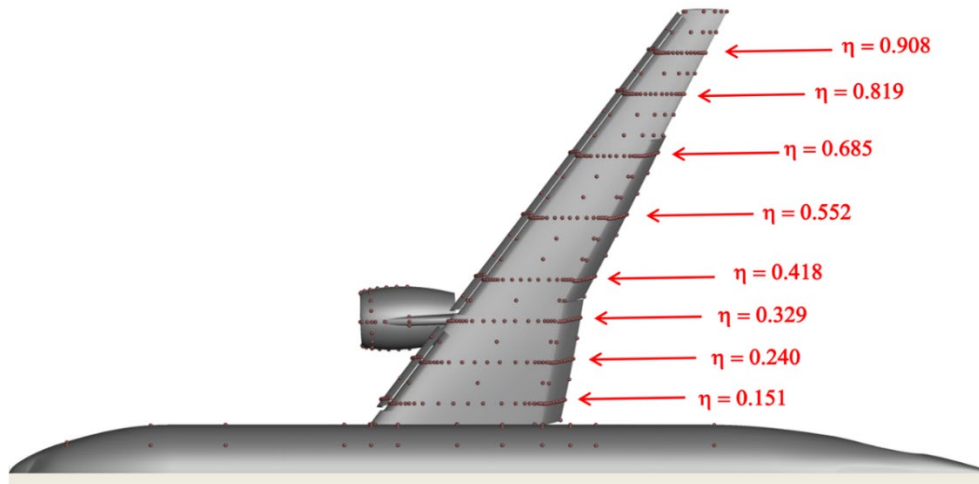

Figure 10: Pressure port layout

VI.   Results

A. Takeoff Configuration Check

Ideally, the starting configuration would have been one of the few tested previously with this model in the 14x22 in order to get a tunnel-to-tunnel comparison. However, another high priority was to get an early look at a takeoff configuration. The limited landing testing in the prior test had revealed that a reasonable landing configuration was achievable, meaning one that produced a rational lift curve, including a reasonable $C_{L,max}$ at a representative stall angle of attack. It would only need to be fine-tuned. No such prior data existed for a takeoff configuration. If anomalous takeoff behavior were to be discovered later in the test, there might not have been adequate time left to address it. In addition, it was desired to scope nacelle chine locations for takeoff so that a common position could be chosen that was effective at both takeoff and landing. In order to avoid having to conduct two large model changes to acquire this initial look at takeoff (landing→takeoff→landing), the test was started with a takeoff configuration.

Fortunately, the starting takeoff configuration produced very reasonable results, except for a small non-linearity in lift in the approach to stall (Figure 11). This was not unlike that seen in the initial results at landing at the 14x22 [11] which was largely remedied by adding, then repositioning the nacelle chine. The initial configuration at the 5mWT included the best chine position from the 14x22. The chine was next tried at two radially lower positions, the lowest of which largely eliminated the non-linearity. With the takeoff configuration de-risked and the chine situation understood, focus moved to the landing configuration tested at NASA.

10
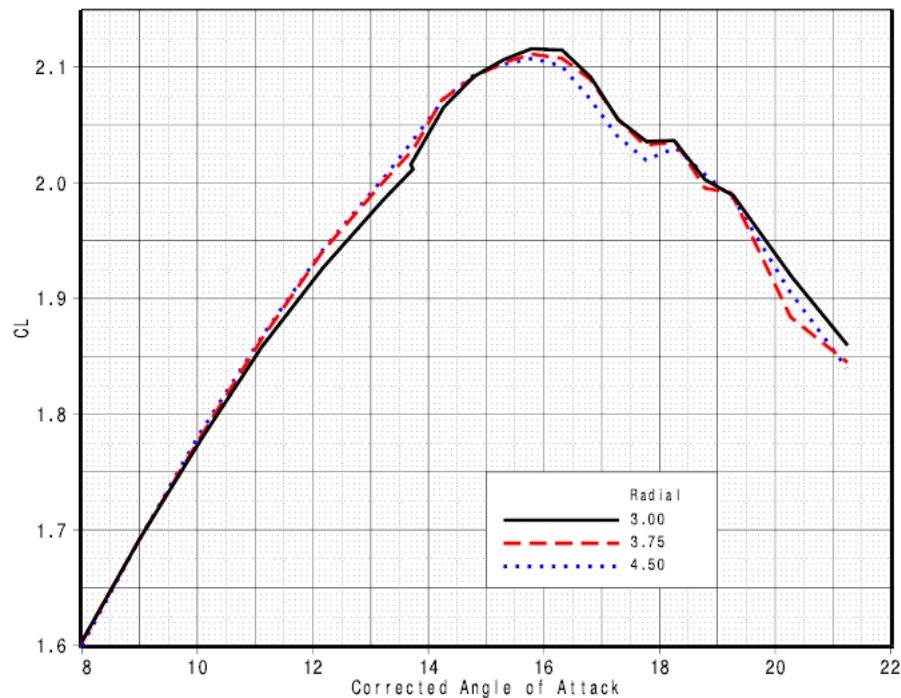
Figure 11: Effect of chine position on lift, takeoff configuration

B. Comparison to 14x22

Lift curve comparisons for the same configuration in both the 14x22 and 5mWT without a nacelle chine, and again with a chine located at the best position from the NASA test, are shown in Figure 12. The lift levels at lower angles of attack were comparable, but the 5mWT data showed an earlier stall resulting in a $C_{L,max}$ that was ~0.08 lower than the data from the 14x22. A comparison of flow visualization data at 18 degrees angle of attack shows that the stall mechanism is different between the two facilities (Figure 13). The stall at the NASA tunnel was driven primarily by weakness emanating from the inboard side of the wing/pylon junction, with some separation starting at the wing/body junction near the wing trailing edge. At the 5mWT, while similar regions of separation develop, the one at the side of body grows much larger at a lower angle of attack and is ultimately the limiting factor for $C_{L,max}$. Diagnostics ensued, such as taping over any potential leakage paths from inside the fuselage - including the peniche labyrinth seal - with no noticeable impact.

While the floor boundary layer was expected to be similar between the two tunnels, the data suggested otherwise. Therefore, attempts were made to change the boundary layer characteristics in the 5mWT in order to see if it had an effect. The easiest way to do so was to turn on the floor blowing capability that had not been used for many years. The system utilizes a slot in the floor near the entrance to the test section as shown in Figure 2. As currently configured, it only provided coarse control of the blowing levels and no ability to measure mass flow levels. It did allow a variation in blowing levels from "low" (B1) to "high" (B6) which enabled changes in the boundary layer profile from small to large as seen in the data from a floor-mounted rake (Figure 14). It is also seen that the effects of the blowing are primarily very near the floor, with high blowing levels resulting in velocities near the wall that are well above the freestream value. The effects of the floor blowing were modest at the low and medium levels, but dramatic at the highest levels (Figure 15). At the high blowing setting, $C_{L,max}$ increased to and even slightly above the levels from the 14x22 facility.

The difference in stall pattern was now linked to differences associated with the floor boundary layer, and the impact of these differences could largely be negated using floor blowing. Unfortunately, the floor blowing could not be precisely controlled, and details like span-wise uniformity were unknown. Therefore, using the blowing would leave many questions about the true tunnel inflow conditions, which is undesirable for CFD correlation. To see if similar effects could be achieved through a repeatable means, vortex generators (VGs) were installed in the contraction

11

throat, approximately 35.5ft upstream of the test section center, as seen in Figure 17. Various patterns of counter-rotating pairs were tested, producing the boundary layer profiles seen in Figure 18 and the corresponding effects on lift seen in Figure 19. While a much fuller boundary layer profile could be achieved with the VG's, the effects on $C_{L,max}$ were modest, as the separation near the body remained the dominant driver for stall. Furthermore, repeatability was an issue as an attempt to repeat the first VG pattern did not provide the same measured boundary layer profile, indicating a high level of sensitivity to the installation.

The inability to find a well understood and repeatable method to eliminate the floor-related effects on stall led to the decision to continue the test primarily without any floor treatments. However, the effects of floor blowing would be examined during portions of the test where it was deemed important to understand the results with the floor issue largely masked. Clearly, there are many unanswered questions regarding the "half model effects" experienced in this test that warrant further exploration in the future.
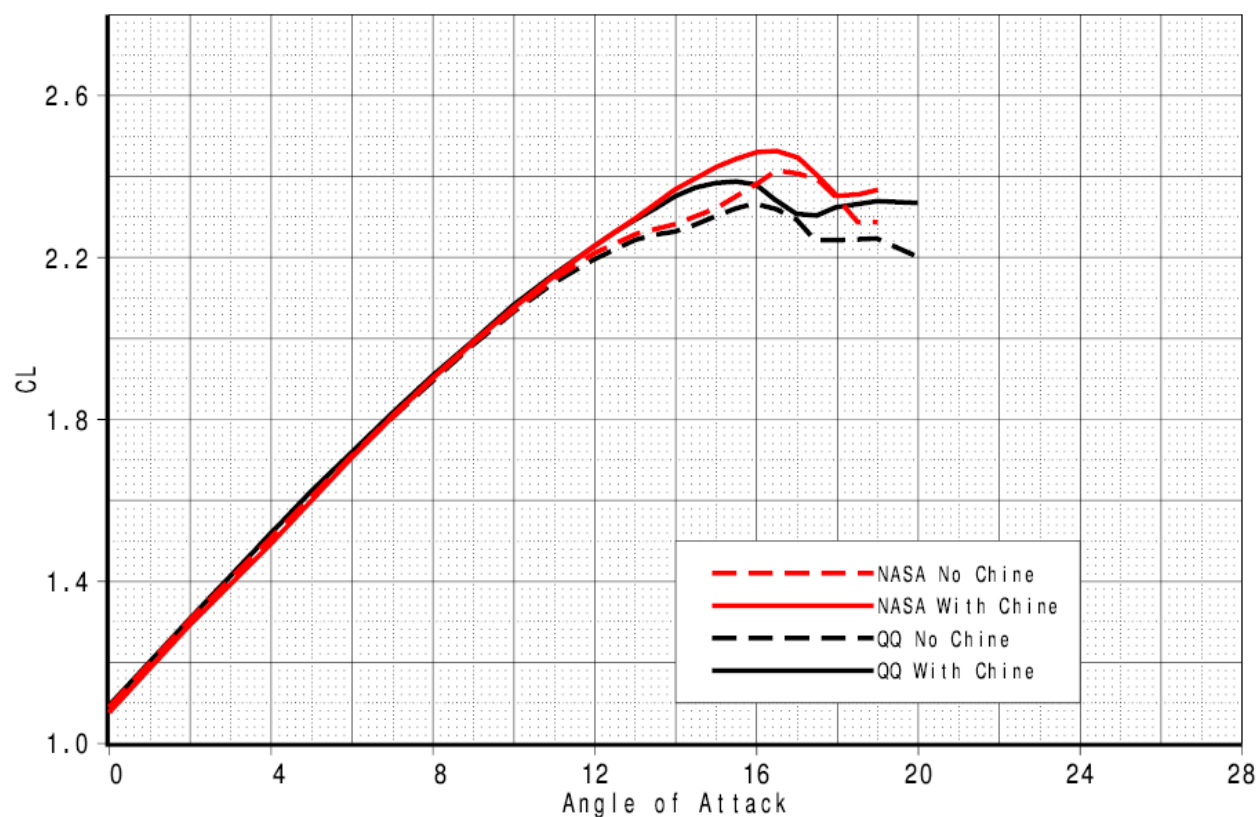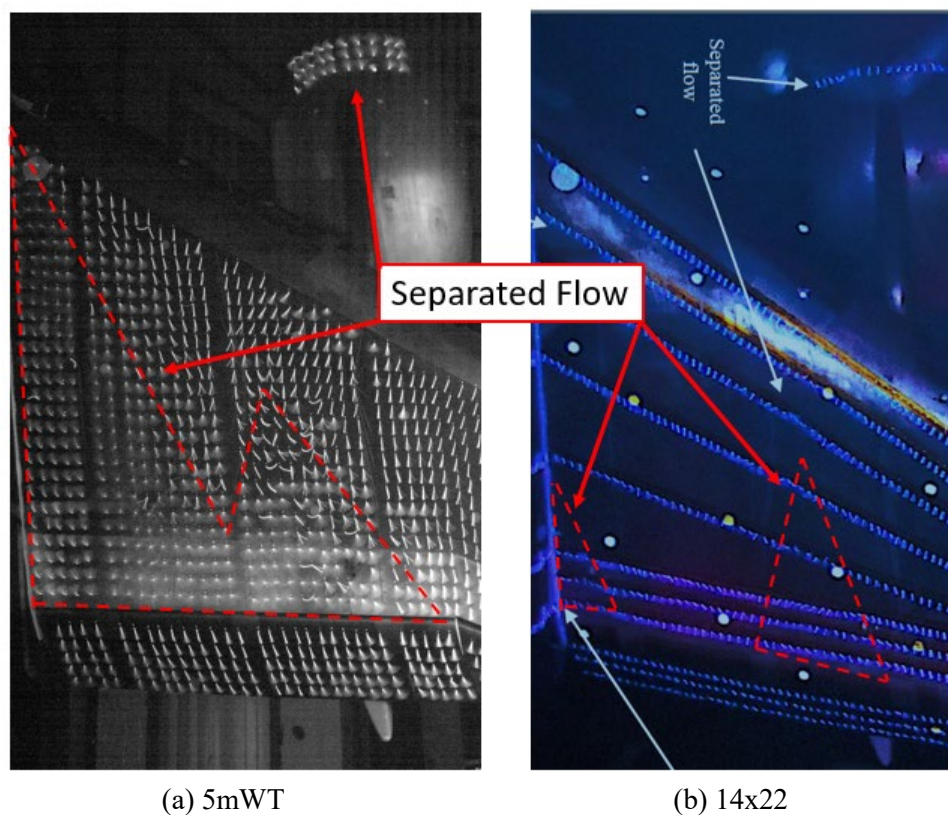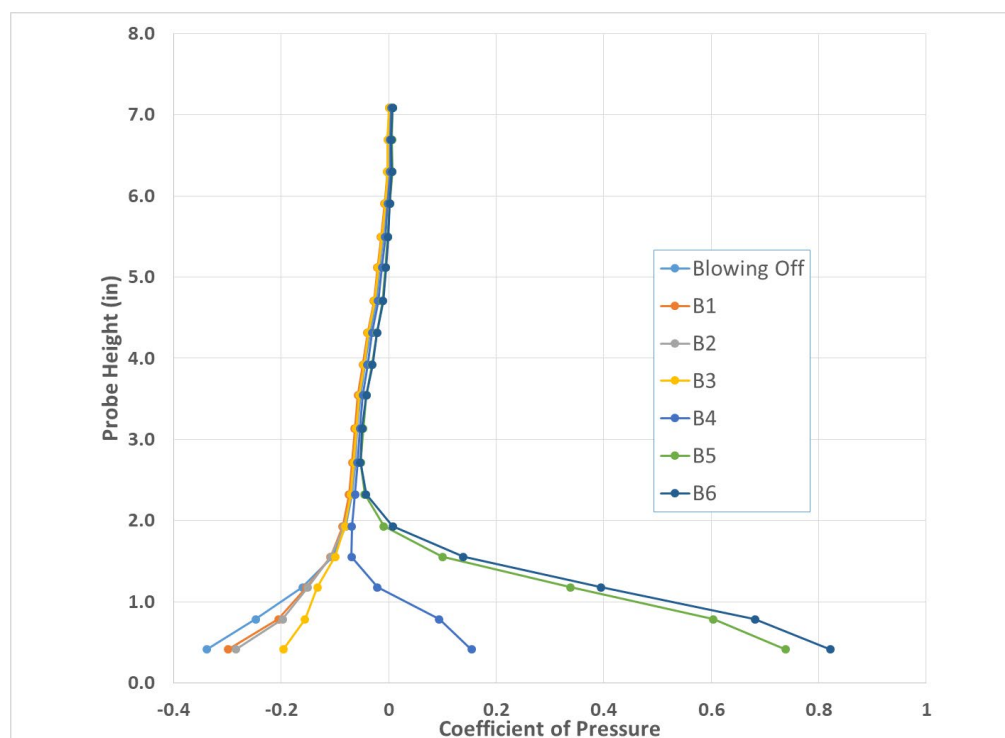

Figure 12: Lift comparison between 5mWT and 14 x 22 Foot test data

<div align="center">(a) 5mWT   (b) 14x22</div>

Figure 13: Comparison of pre-test nominal landing configuration surface visualization, α_U=18°
(14x22 image from [14])

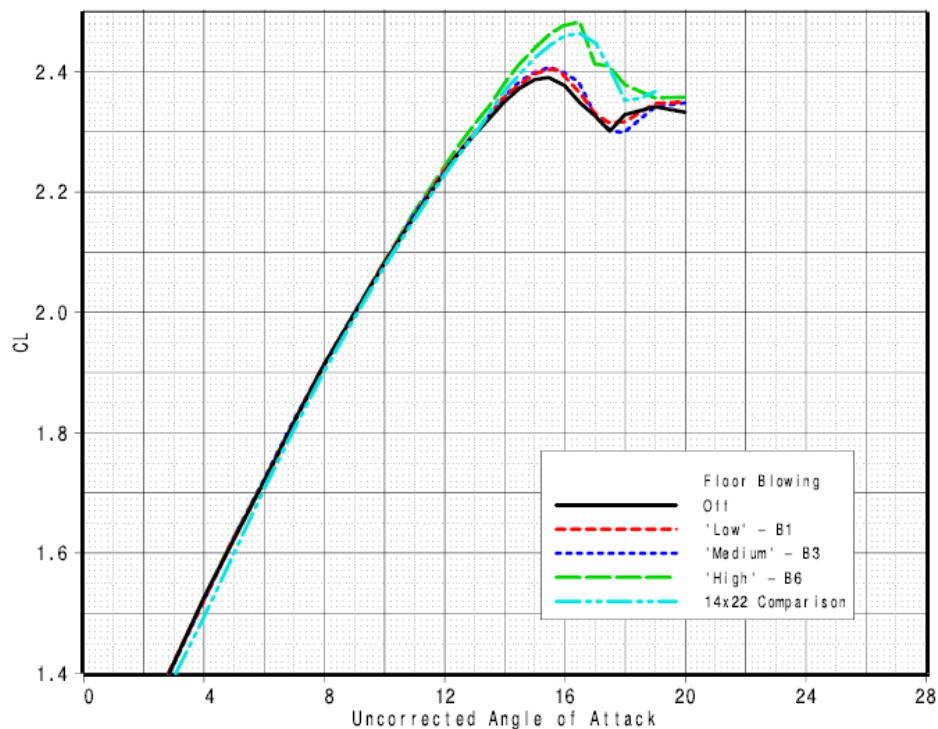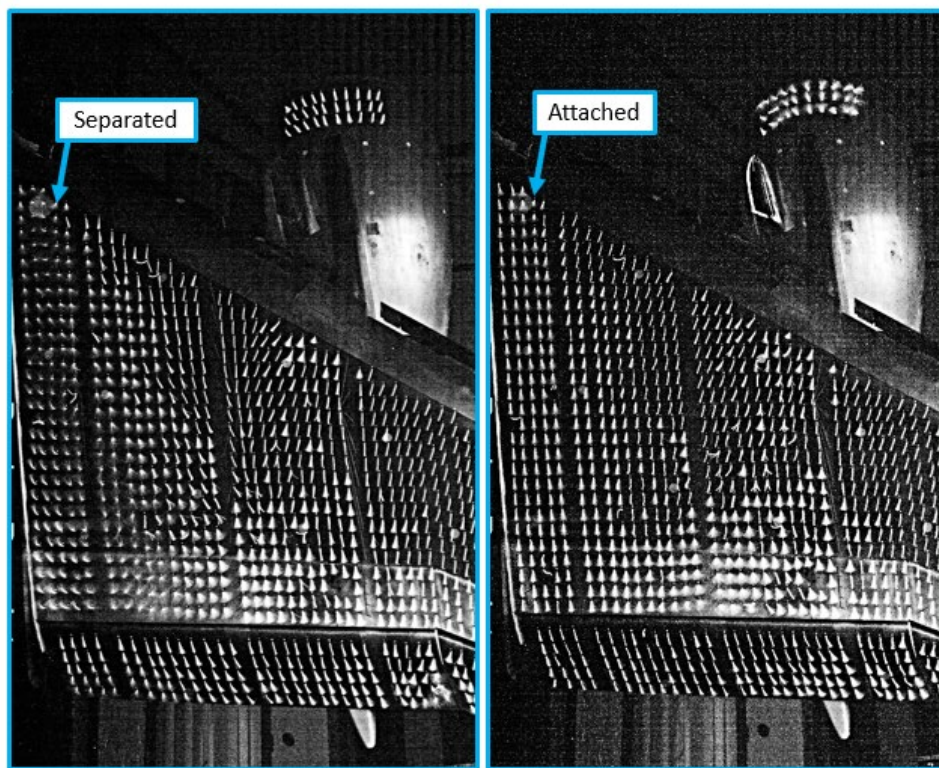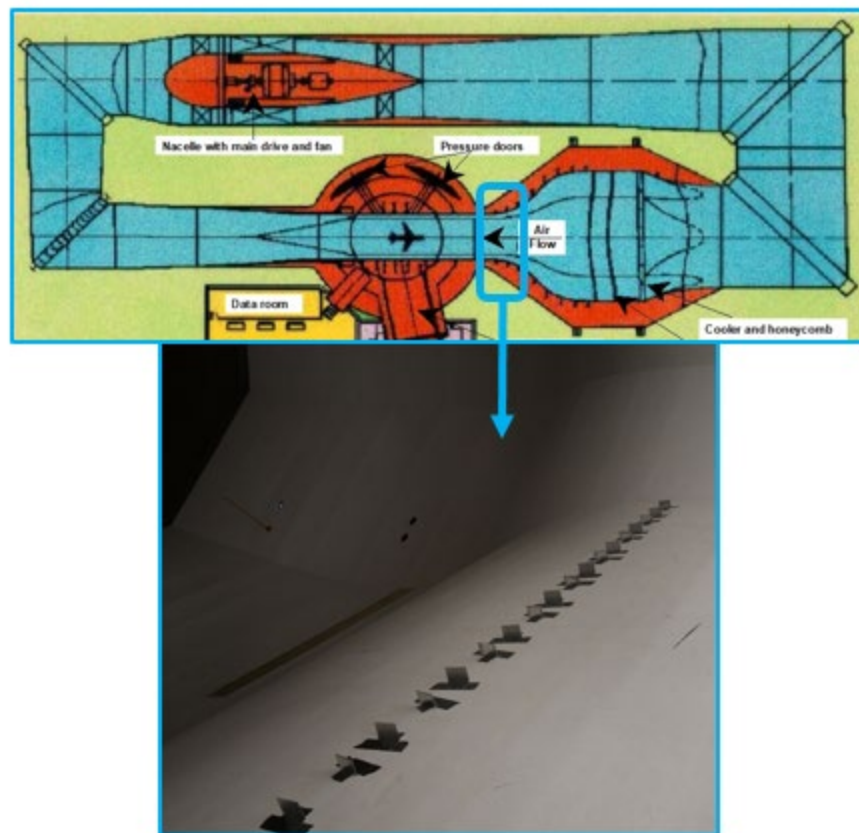

Figure 14: Boundary layer profiles with floor blowing

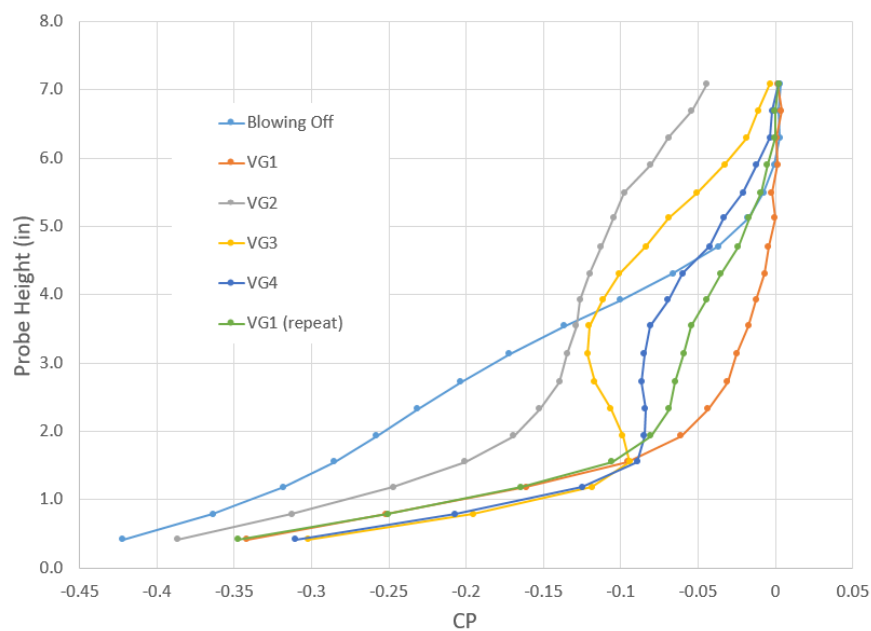**Figure 15: Effect of floor blowing on lift**

(a) Floor flowing off   **(b) Floor blowing 'high'**

Figure 16: Blowing-off vs blowing-on flow visualization, α = 17°

Figure 17: Floor VGs

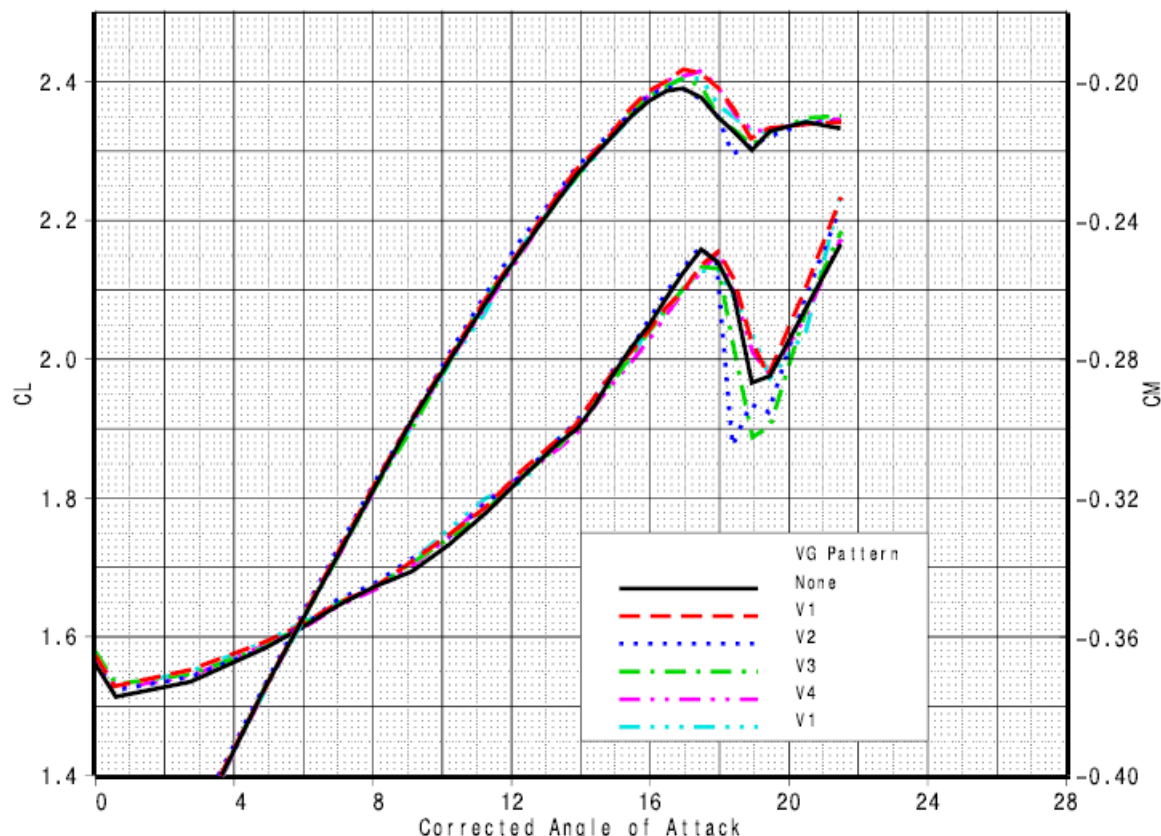**Figure 18: Effect of VGs on boundary layer**

Figure 19: Effect of floor VGs on lift and pitching moment

C. Landing Configuration Development

1. Trailing Edge

The inboard and outboard flap positioning were varied independently to assess sensitivities to angle, gap and overlap. Primarily due to its increased sweep, the outboard flap boundary layer is less healthy at a given angle than the inboard flap. Because of this, the outboard flap angle was set three degrees lower than that of the inboard flap for the landing configuration to help compensate. (Three degrees was the increment between available bracket angles for the wind tunnel model.) Figure 20 shows photos of the mini-tufts on the flaps through a progression of flap angles at both 6 degrees angle of attack and 17 degrees (near stall). The increase in separation with flap angle can be seen at the lower angle of attack, beginning behind flap support fairings and near the flap junction. Flap loading generally decreases at higher angles of attack, with the result here being dramatically reduced separation as shown in the mini-tufts at the higher angle of attack. It should be noted that only selected results are shown here and throughout this test summary. While the intent is to eventually release all of the data, much will be held in reserve in order to best support CFD collaboration activities such as workshops.

16

$\alpha_U = 6°$

$\alpha_U = 17°$
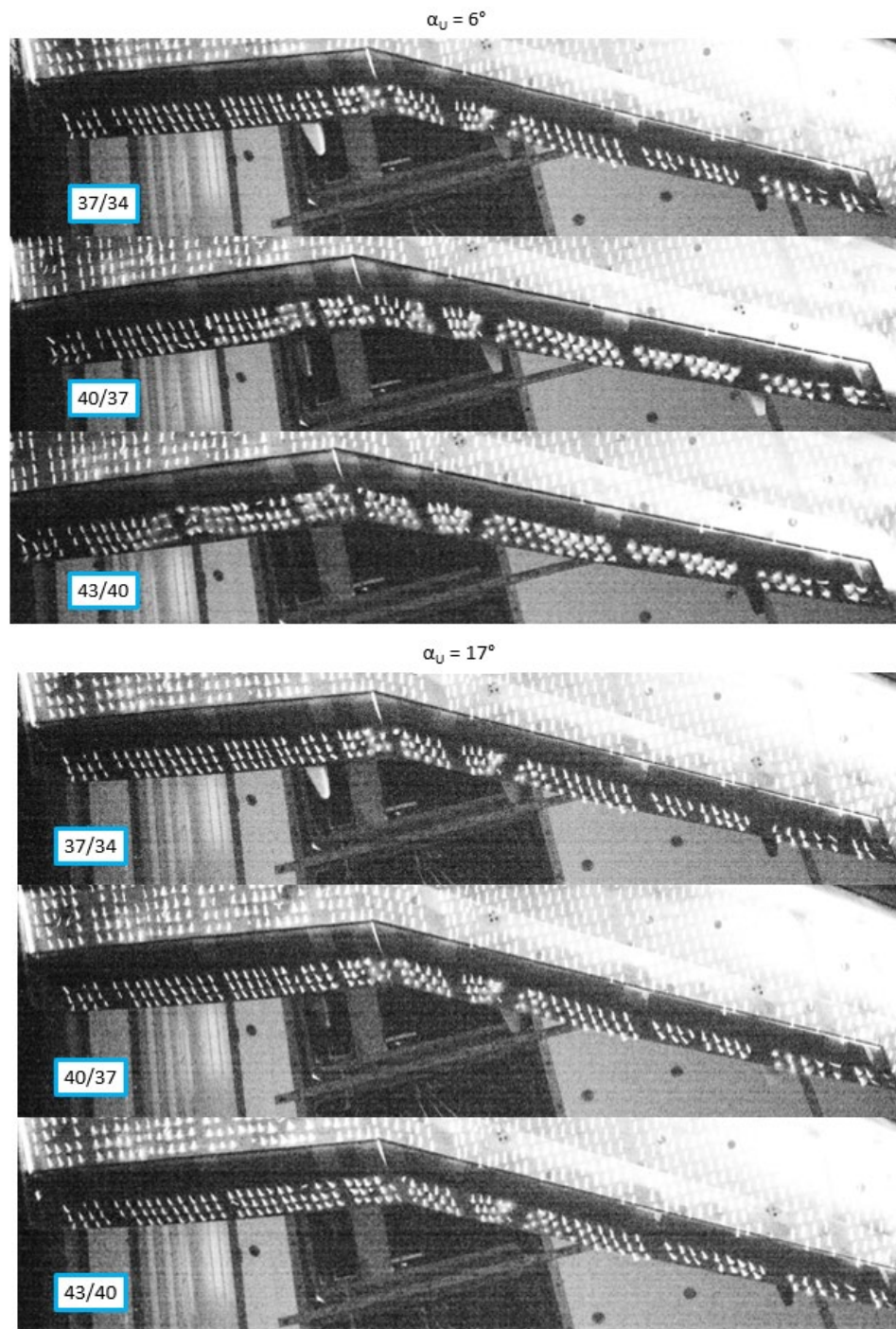
Figure 20: Trailing edge separation, landing configuration

2. Leading Edge

The positioning of the inboard and outboard slats was also independently varied. The high angle of attack performance of the inboard wing was dominated by separation near the body when no floor blowing was used, making the effects of leading edge positioning on the pylon driven separation more difficult to deduce. Therefore, the inboard slat positioning study was conducted with a combination of floor blowing on and off. In the end, better overall

performance was obtained by increasing the height of the slat, but the angle and gap did not change from pre-test values. The increase in height also decreased the sensitivity to the floor boundary layer issue, reducing the difference between the lift curves obtained with and without blowing (Figure 21).

Even with the most powerful leading edge that was able to be configured with the existing parts, the inboard wing was always the limiting factor which determined when the wing stalled. Therefore, as suspected, performance sensitivity to variations in outboard slat positioning was small. Ultimately, a position incorporating a higher height was chosen to enable the inboard and outboard slats to be connected later in the test when the nacelle and pylon were removed.
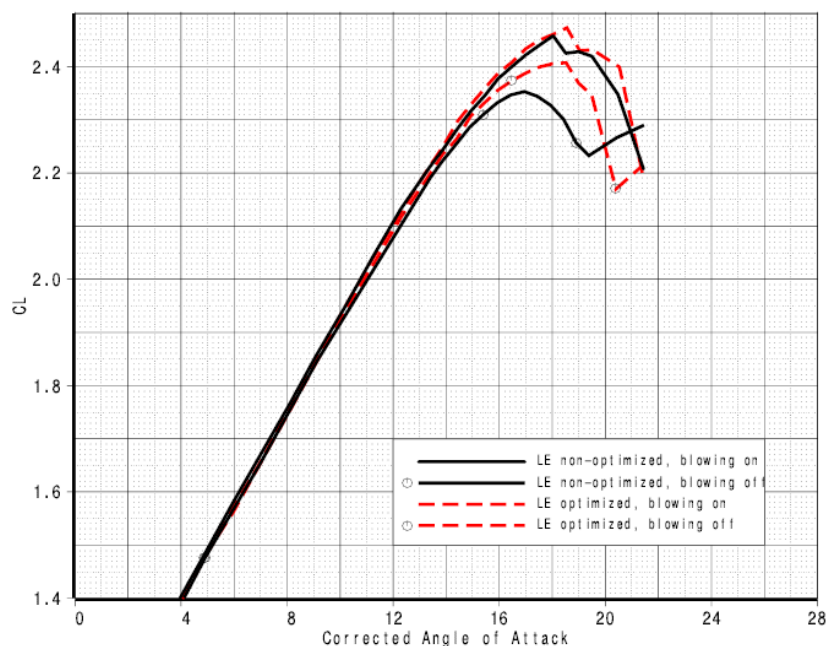
Figure 21: Reduced floor blowing effects for stronger leading edge

3. Nacelle chine placement

Nacelle chines can be used in conjunction with leading edge devices to control flow over the wing and delay the onset of stall. During this test, limited variation of chine size and positioning was explored to see if markedly better performance could be achieved. The only significant $C_{L,max}$ sensitivity was associated with a much larger chine. However, the size was not representative of those found on most commercial airliners, so the starting medium-sized chine was maintained. The final chine position combines the radial position of the takeoff position arrived at previously with a more forward longitudinal placement. This position ultimately satisfied requirements at both takeoff and landing configurations.

4. Nacelle cowl impact

An undesirable feature was identified in the lift curve in the form of a 'notch' near $C_{L,max}$ (Figure 22). It was triggered by separation starting at the lip of the nacelle which can be seen in the mini-tufts in Figure 23 at position "b". This separation was detected by CFD during the design of the geometry, but occurred slightly after wing stall, so no changes were made to the nacelle, which was carried over from the High Speed CRM geometry set. This phenomenon didn't impact the $C_{L,max}$ levels dramatically, but did add more complexity to an already complex flow field near stall. To ensure that the lift curve notch was a result of the cowl separation, one run was made with a temporary modification to the upper inlet lip of the nacelle with the intention to delay this separation. Figure 22 shows that this was achieved and the notch in the lift curve disappeared, indicated at position "d". It was therefore decided that the nacelle cowl lip should be modified for the final released geometry in such a way that the cowl separation is pushed a few degrees higher in angle of attack.
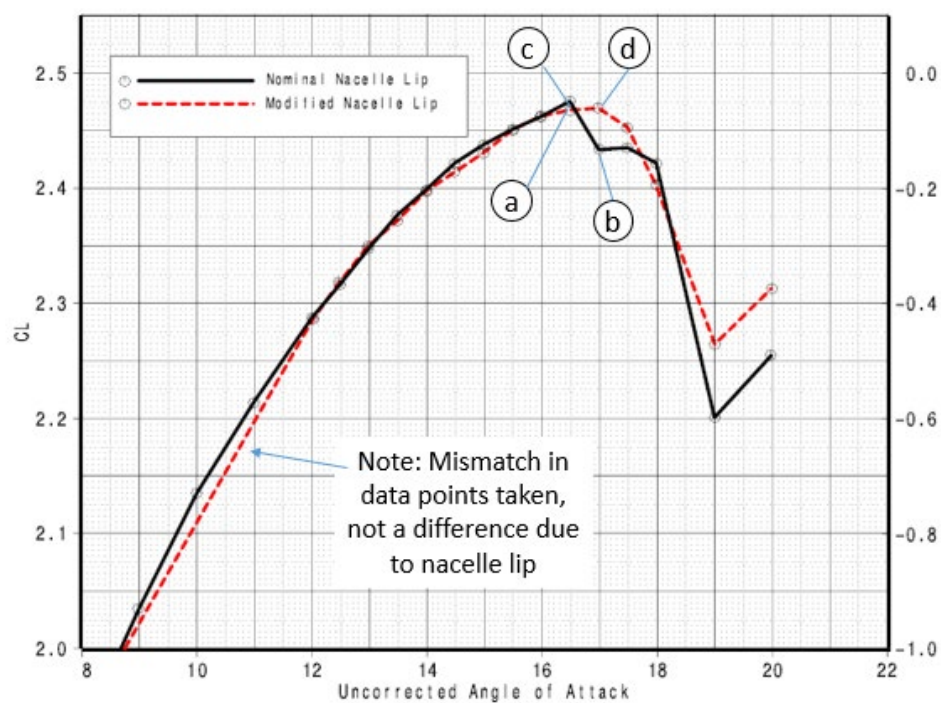
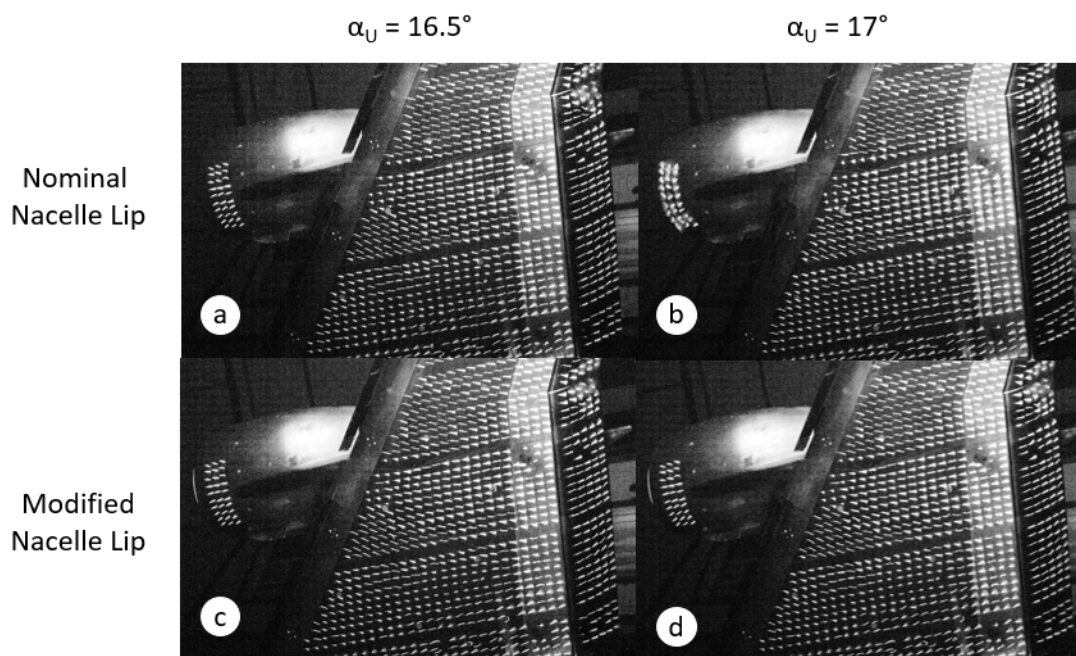**Figure 22: Effect of nacelle lip modification on lift**

$\alpha_U = 16.5°$ $\alpha_U = 17°$

Figure 23: Flow visualization of effect of nacelle lip modification

19

5. Reynolds number effects on landing configuration

Variations in Reynolds number can impact the effectiveness of both leading edge and trailing edge devices. Optimization at low Reynolds number will often result in different positioning than if it were done at higher Reynolds number. Given that the most relevant answers are those at flight Reynolds number, it is desirable to optimize for the highest Reynolds number possible. However, for the CRM-HL ecosystem, it is expected that these configurations will be tested across a wide range of Reynolds number, so this must be taken into account in reference configuration selection. A strategy for dealing with this issue is described in [12]. In this test, it was desired to gather data for the widest range of Reynolds numbers possible in order to support this strategy.

The model was designed for atmospheric testing at Mach numbers up to 0.26 to cover the range for takeoff testing. Because landing was run at Mach 0.20, which represents a much lower dynamic pressure, this allowed for the 5mWT pressurization to be used to achieve a higher Reynolds number while staying within the limits of the model design. Additionally the full range of tunnel pressurization could be achieved at Mach 0.15. Figure 24 shows some results of this testing.
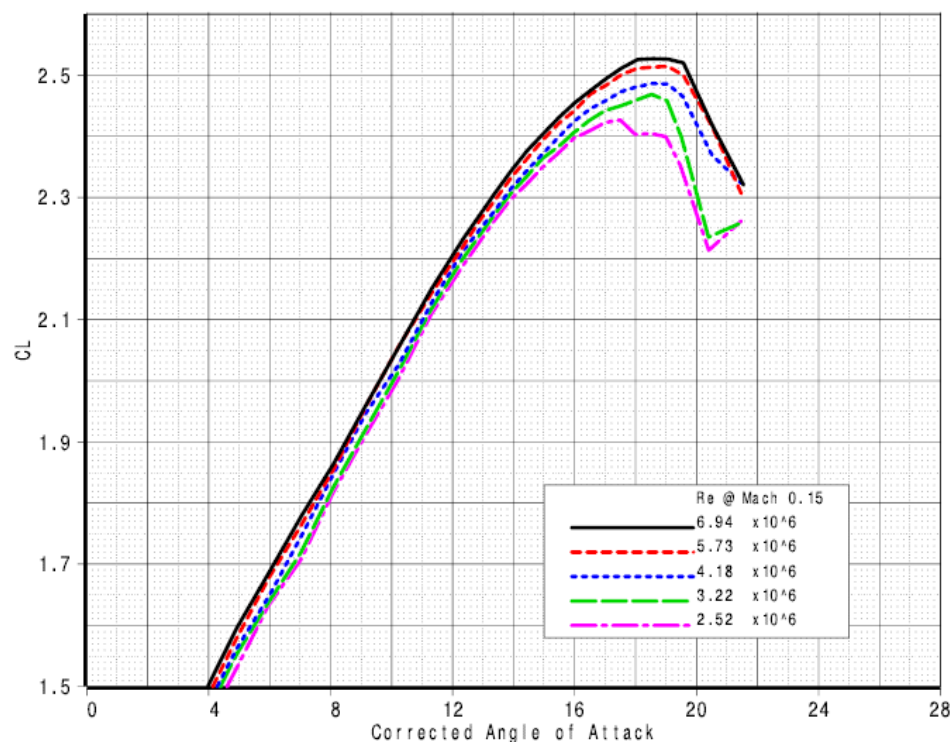

Figure 24: Effect of Reynolds number on lift, landing configuration

D. Takeoff Configuration Development

1. Leading edge

A range of positions were tested for the leading edge, with similar strategy and issues as in the landing configuration. There was relatively little C_{Lmax} variation across the range of positions tested, with no anomalous behavior observed. The exploration included configurations with the slats sealed to the WUSS. While there was a small C_{Lmax} penalty for doing so, the sealed case was chosen for the reference takeoff leading edge configuration. It presents a different – and simpler – flow field for future computational exercises, as it eliminates the leading edge bracket wake effects, and the modeling challenges associated with them, that would normally be present with a gapped slat. As with landing, some of the takeoff leading edge testing was conducted with the floor blowing turned on. Figure 25 shows the effect of floor blowing on the chosen configuration.
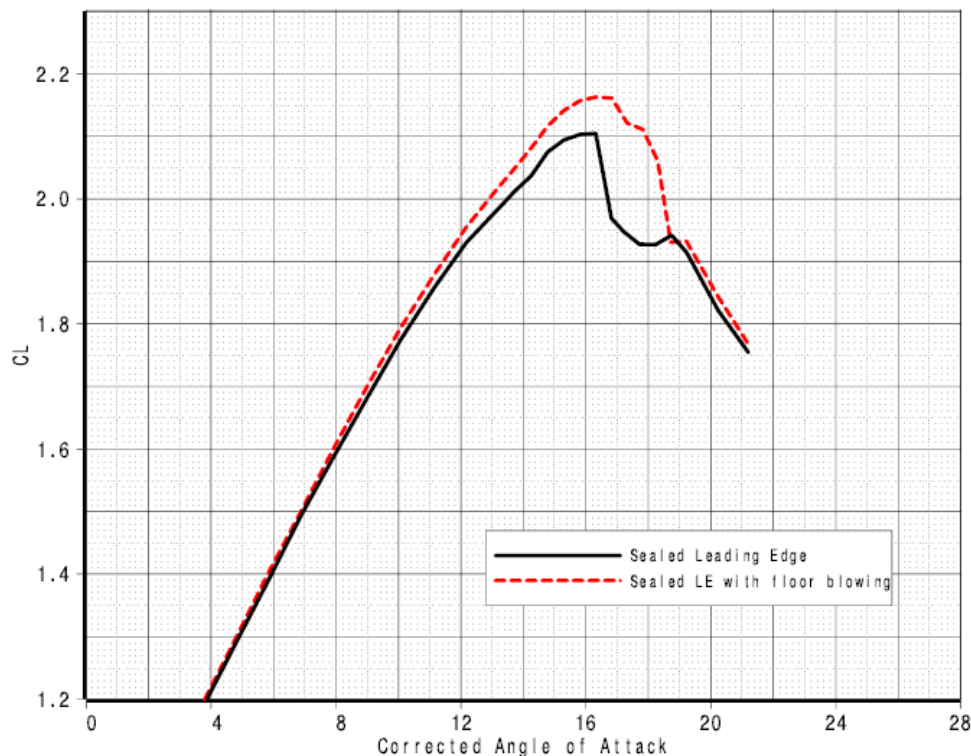
Figure 25: Effect of floor blowing with sealed slat, takeoff configuration

2. Trailing edge

The test plan originally included testing for a shallow takeoff flap deflection (10°) and a deeper takeoff flap deflection (25°). However, fitting issues and general schedule pressure resulted in only the deeper takeoff deflection being tested. Gap sensitivity data were collected, but ultimately the pre-test nominal setting was kept for the reference configuration.

**E. UV Oil Studies for Landing Configuration**

While the mini-tuft pictures are valuable and are easy to capture in non-intrusive fashion during the course of testing, much more detail can be seen using UV oil surface flow visualization. These pictures are often very useful in comparisons with CFD in order to see if the computations are picking up the details near the surface of the model. However, this requires dedicated testing to allow for application of the oil, running the tunnel at one angle of attack, taking images and then cleaning up the oil. The process is then repeated for all desired angles of attack. In addition, prior to applying the oil, all of the mini-tufts need to be removed and all pressure ports need to be taped over to prevent contamination. Due to these factors, a few days were set aside at the end of the test to capture UV-oil surface flow visualization data. All data were collected with the landing configuration, with and without the nacelle and pylon. Some variation of Reynolds number was also explored. An example of how floor blowing alters the inboard wing flow field near stall is shown in Figure 26. In this comparison, the flow separation observed at the side-of-body with no floor blowing is essentially removed when floor blowing is turned on using the high (B6) boundary layer profile provided in Figure 14. Note that the flow outboard from this location is largely unaffected by the use of floor blowing.
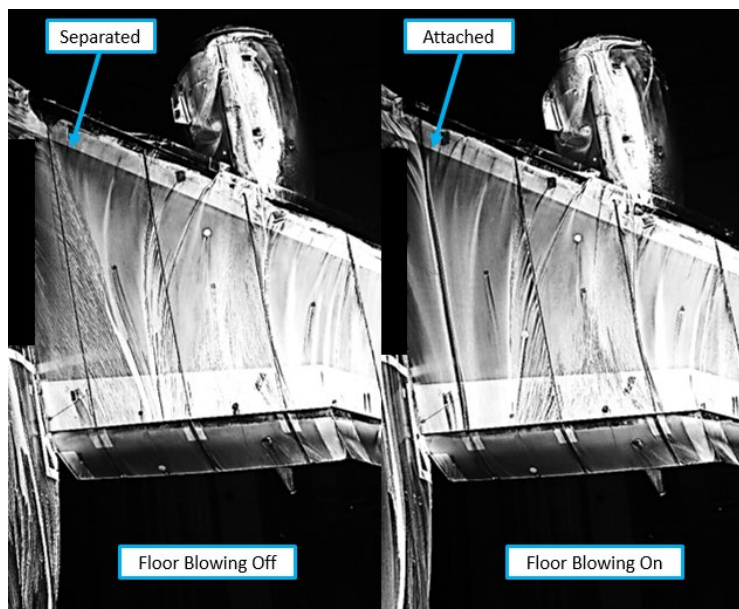
Figure 26: Floor blowing comparison with UV oil flow

F. Nacelle and Pylon Removed

To obtain data for a configuration without the engine installation, the nacelle and pylon were removed, leaving a discontinuous slat across the nacelle region. UV oil flow data was collected, and a pitch sweep for balance data was performed. Then an additional set of parts was installed that connected the inboard and outboard WUSS and slats to create a continuous leading edge. Additional pitch sweeps were performed, some with varying Reynolds number and some with floor blowing. UV oil data was also gathered on this configuration. Examples are shown in Figure 27, at both a low and high angle attack.
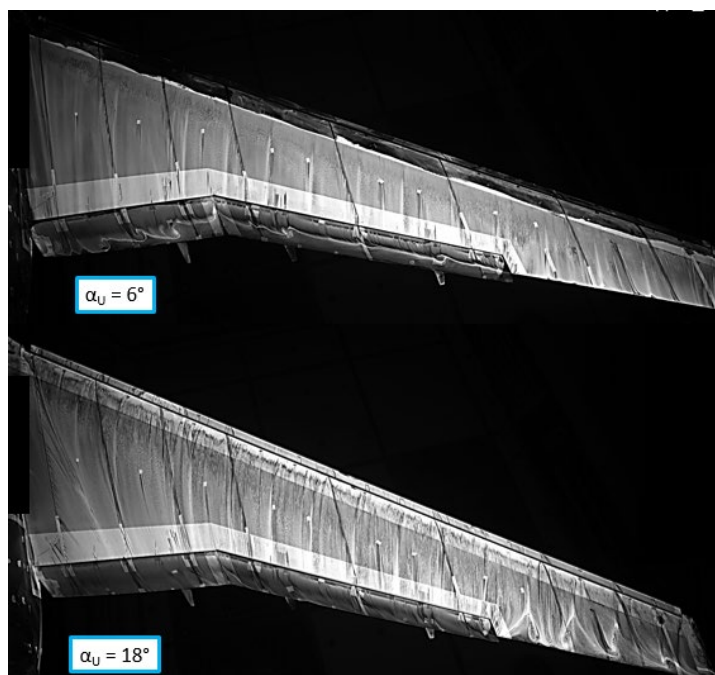
Figure 27: UV oil flow with continuous leading edge

G. Particle Image Velocimetry and Model Deformation Measurement

This test was also used as an opportunity to trial two new systems in the 5mWT. A PIV system was demonstrated, exploring positioning of the laser and cameras within the physical constraints behind the tunnel walls. Due to these constraints, the system was set up in a symmetric backscatter arrangement, i.e. the laser and cameras were on the same side of the measurement plane with the cameras on either side of the laser (Figure 28). Seeding trials with Di-Ethyl-Hexyl-Sebacat (DEHS) were run to determine appropriate levels for filling the circuit from downstream of the model to result in optimum levels of seeding at the model. Tests were successfully performed at 1, 2, and 3 atmospheres, and up to Mach 0.26, but not at the highest pressure and Mach number concurrently due to load issues with the model.

An MDM system was also successfully demonstrated, exploring the position of the most effective model target images (as depicted in Figure 5 and Figure 6) and camera locations. The targets were illuminated with infrared narrow bandwidth illumination lights and the cameras were filtered for 850nm. Initial results are forthcoming.
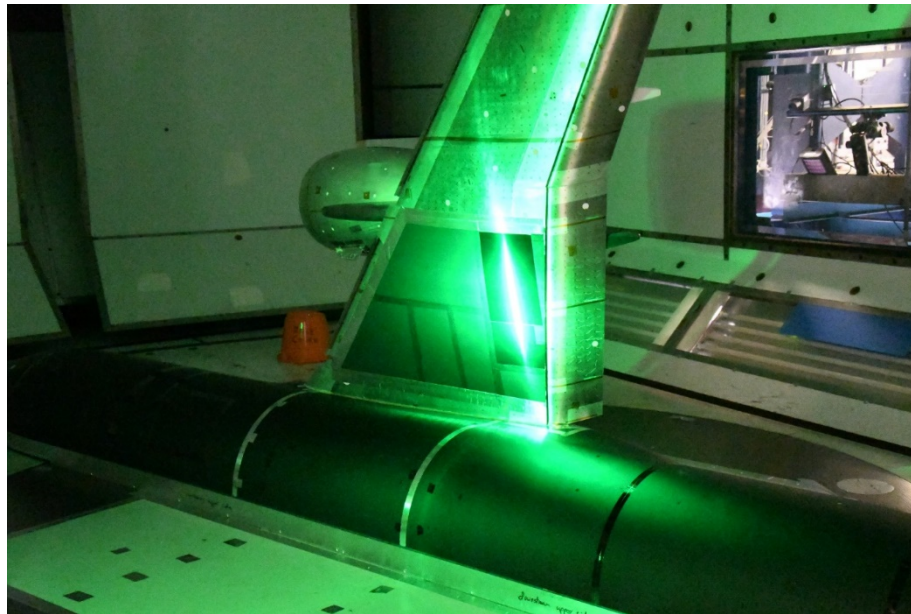

Figure 28: PIV setup

VII.   Conclusion

A summary and selected results from wind tunnel testing of the NASA 10% CRM-HL at the QinetiQ 5m pressurized low-speed wind tunnel have been presented. A large amount of high-quality force, moment, pressure, and flow visualization data were gathered to help define the reference configurations and variations thereof which will be very useful for future CFD validation. A good set of data were acquired to develop a strategy for how to adapt the landing reference configuration for different Reynolds number experiments. Data were gathered to isolate effects of different components such as landing gear, horizontal tail, and nacelle/pylon.

A facility-to-facility difference was discovered to be much larger than expected, and was due to the effects of the floor boundary layer on a half-model. Methods were investigated for assessing and minimizing the impact of these differences. Floor blowing and floor VGs both had an impact on the boundary layer and therefore on the model aerodynamics, but neither method was fully understood or repeatable. With the growing ecosystem of wind tunnel tests, these effects require further study, which will contribute to improving wind tunnel methods and CFD validation.

Acknowledgments

References

[1] Slotnick, J., Khodadoust, A., Alonso, J., Darmofal, D., Gropp, W., Lurie, E., and Mavriplis, D., "CFD Vision 2030 Study: A Path to Revolutionary Computational Aerosciences, NASA/CR-2014-218178, March 2014; https://ntrs.nasa.gov/archive/nasa/casi.ntrs.nasa.gov/20140003093.pdf.

[2] Rumsey, C. L., Slotnick, J. P., and Sclafani, A. J., "Overview of Summary of the Third AIAA High Lift Prediction Workshop," AIAA Paper 2018-1258, *AIAA SciTech Forum,* Kissimmee, FL January 8-12, 2018

[3] Meredith, P. T., "Viscous Phenomena Affecting High-Lift Systems and Suggestions for Future CFD Development," AGARD-CP-515, Paper 19, September 1993

[4] Ewald, B.F.R. (ed), "Wind Tunnel Wall Correction", AGARD-AG-336, October 1998.

[5] Earnshaw, P. B., Green, A. R., Hardy, B.C., and Jelly, A. H., "A Study of the Use of Half-Models in High-Lift Wind Tunnel Testing," AGARD-CP-515, Paper 20, September 1993

[6] Woodward, D.S., Hardy, B. C., and Ashill, P. R., "Some Types of Scale Effect in Low-Speed, High-Lift Flows," ICAS Paper 4.9.3, Jerusalem, 1988

[7] Clark, A. M., Slotnick, J. P., Taylor, N., and Rumsey, C. L., "Requirements and Challenges for CFD Validation using the High-Lift Common Research Model,", AIAA Paper 2020-2772*, AIAA Aviation 2020 Forum*

[8] Rivers, M. B., "NASA Common Research Model: A History and Future Plans," AIAA Paper 2019-3725, June 2019

[9] Lacy, D. S. and Sclafani, A. J., "Development of the High Lift Common Research Model (HL-CRM): A Representative High Lift Configuration for Transonic Transports," AIAA Paper 2016-0308, 54th AIAA Aerospace Sciences Meeting, San Diego, CA, January 4-8, 2016.

[10] Lin, J.C., Melton, L. P., Viken, S. A., Andino, M. Y., Koklu, M., Hannon, J. A., and Vatsa, V.N., "High Lift Common Research Model for Wind Tunnel Testing: An Active Flow Control Perspective," AIAA Paper 2017-0319, *AIAA SciTech Forum,* Grapevine, TX, January 9-13, 2017

[11] Lin, J.C., Melton, L. P., Hannon, J. A., Andino, M. Y., Koklu, M., Paschal, K. B., and Vatsa, V. N., "Wind Tunnel Testing of Active Flow Control on High Lift Common Research Model," AIAA Paper 2019-3723, *AIAA Aviation 2019 Forum*, Dallas, TX, June 17-21, 2019

[12] Lacy, D. S, "Definition of Initial Landing and Takeoff Reference Configurations for the High Lift Common Research Model (CRM-HL)" AIAA Paper 2020-2771, *AIAA Aviation 2020 Forum*

[13] Woodward, D.S., Francois, G. and Taylor, N., "The Aerodynamic and Structural Design of the DRA 5-Metre and ONERA F1 Low-Speed Pressurised Wind Tunnels", AGARD-CP-585, Paper 4, June 1997.

[14] Koklu, M., Lin, J. C., Hannon, J. A., Melton, L. P., Andino, M. Y., Paschal, K. B., and Vatsa, V. N., "Surface Flow Visualization of the High-Lift Common Research Model," AIAA Paper 2019-3727, June 2019